


Peristaltic Flow in Compressible, Ideal Magnetohydrodynamics: A Mechanism For Solar Spicules

D. Tsiklauri  *

Joule Physics Laboratory, School of Science, Engineering and Environment,
University of Salford, Manchester, M5 4WT, United Kingdom

(Dated: June 9, 2026)

We present analytical model for peristaltic transport within compressible, ideal magnetohydrodynamics (MHD). By employing small-amplitude perturbation expansion, under thin-tube long-wavelength approximation with a uniform axial background magnetic field, we study non-linear coupling between thermodynamic pressure variations and Maxwell's magnetic tension stresses. The resulting net time-averaged volumetric flow rate $\langle Q \rangle$ is calculated. When applied to solar chromospheric spicules under equipartition constraints ($\beta \sim 1$), where sound speed matches the Alfvén speed, we find $\langle Q \rangle = 4\epsilon^2 / (M^2 - 1)$. Because the denominator remains positive across all operational supersonic Mach numbers ($M \approx 2-10$), upward-propagating mechanical disturbances drive a highly directional, collimated upward flow which we interpret as a spicule. Estimates show that for observationally realistic magnetosonic waves with amplitudes of $\approx 10\%$, the peristaltic mechanism generates a localized mass flux ≈ 100 times that of solar wind. We propose an explicit observational signature of this mechanism, wherein the launch of individual spicular jets is directly preceded by magnetosonic wave trains detectable as localized intensity modulations. Beyond solar chromospheric application, the model may be applicable to traveling magnetic field pinches in laboratory plasma devices and astrophysical mass-loading processes in stellar winds and inner regions of magnetized accretion disks.

I. INTRODUCTION

The peristaltic mechanism is a fundamental fluid-dynamic flow generated by a progressive wave of cross-sectional area contraction or expansion moving along the flexible wall of a fluid-filled distensible tube [1]. Historically, this phenomenon has been extensively investigated across an array of vital biological [2] and engineering applications, including the physiological pumping of urine through the ureters, digestive transit, blood transport in heart-lung machinery, and the sanitary transport of corrosive fluids [3]. On macroscopic geophysical and environmental scales, peristaltic flows are frequently utilized to govern non-linear fluid streams passing through porous media domains [4], such as groundwater management, oil extraction mechanics, and plant nutrient transport channels [5]. Despite its well-documented use in industrial, environmental, geophysical and biological applications, the implementation of peristaltic transport models has found less use in astrophysical plasma contexts. However, this is a clear oversight because waves travelling on boundaries of magnetic flux tubes are found in many solar and astrophysical situations. This paper attempts to fill this void by utilizing a closed, analytical magnetohydrodynamic (MHD) framework to study wave-driven mass transport in structured solar chromospheric magnetic flux tubes. We therefore propose a peristaltic flow in compressible, ideal MHD as a possible mechanism for solar chromospheric spicules.

The foundation of traditional hydromagnetic pumping models traces its origins back to the early fluid mechanic frameworks established by Shapiro, Jaffrin, and Weinberg [6]. However, the overarching history of this propulsive mechanism originates from the seminal *ex vivo* experimental milestones executed by British physiologists at the turn of the twentieth century. Working in London, Bayliss and Starling [1, 7]

provided the first systematic description of the myenteric reflex and gut peristalsis, formulating the classical "law of the intestine" to mathematically map how localized wall contractions drive forward fluid masses [1]. While those pioneering physiological works assumed an incompressible, viscous, and field-free domain, clearly, modern solar environments require an extension into supersonic, compressible, and ideally conducting magnetoacoustic physics. To contextualize the development of peristaltic pumping theory, the literature is divided into two distinct historical phases, establishing how the present model builds upon these foundational steps: (i) Shapiro, Jaffrin, and Weinberg [6] established the first rigorous mathematical framework for peristaltic transport in 1969. However, their classical formulation was strictly restricted to Newtonian, *incompressible* fluids at low Reynolds numbers. Under their assumptions, the normalized net time-averaged volumetric flow rate is an invariant geometric property ($\langle Q \rangle = \epsilon^2$), completely devoid of acoustic wave interactions, structural phase lags, or wavespeed-driven singularities. Their non-linear expansion of the pressure gradient follows classic compressible flow relationships [8]. (ii) Following the foundational compressible flow framework established by Shapiro [8], Aarts and Ooms [4] pioneered the study of *compressible* viscous liquids induced by traveling waves in porous media. By evaluating the non-linear expansion of the pressure gradient, they were the first to uncover internal acoustic streaming within a peristaltic system – a phenomenon completely absent in the classical incompressible theory. Motivated by applications such as ultrasound-enhanced oil recovery, they were the first to demonstrate that fluid compressibility introduces internal acoustic streaming. This compressibility creates structural phase shifts and non-linear pressure gradients that can drastically amplify or suppress net forward transport phenomena that the incompressible Shapiro model could not predict. (iii) Consequently, [4] were not the first to model peristaltic pumping, but they were the first to identify the profound role of fluid compressibility. The analytical framework derived in this manuscript

* D.Tsiklauri@salford.ac.uk

bridges these two milestones. By extending the compressible traveling wave paradigm into the ideal *magnetohydrodynamic* regime, this work uncovers how a uniform background magnetic field introduces Alfvénic stiffness to directly compete with and regulate the acoustic-streaming resonances first discovered by Aarts and Ooms [4].

The mathematical abstraction of peristaltic transport has similarly expanded beyond classical Newtonian limits to incorporate complex fluid rheologies and dynamic boundaries. Notably, Tsiklauri and Beresnev [9] evaluated non-Newtonian effects within the peristaltic pumping framework by modeling a Maxwellian fluid inside a circular tube driven by a transverse wall wave. Their formulation unraveled unique transport mechanics in extreme regimes, showcasing that viscoelastic properties can induce a localized retrograde flow directed entirely opposite to the guiding wall wave propagation vector. Furthermore, the dynamic response of driven conduit systems is known to be highly sensitive to the movement of the structural boundaries themselves. Tsiklauri and Beresnev [10] explored this behavior by checking the response of a viscoelastic fluid confined within a longitudinally vibrating cylindrical channel. Their exact frequency-domain analysis revealed dramatic resonant enhancements in fluid throughput at specific threshold frequencies, proving that coordinated boundary oscillations can fundamentally optimize or alter net transport profiles. While these foundational models demonstrate the intricate roles of elasticity, boundary vibrations, and non-Newtonian backflows in terrestrial settings, our ideal MHD formulation examines how a global magnetosonic travelling wave functions as a steady propulsion engine under compressible, high-velocity astrophysical limits.

To establish the physical foundation for our model, and to study *one* of the possible applications, we map our analytical transport mechanics directly onto the observational and theoretical realities of solar spicules. Solar spicules are high-velocity, jet-like plasma structures ubiquitously observed protruding from the solar chromosphere into the million-degree corona [11]. High-resolution spaceborne observations, notably using instruments onboard the *Hinode* spacecraft [12], reveal that these structures possess an elongated aspect ratio with a typical radius $R \approx 100\text{--}150$ km spanning lengths L over several thousand kilometers. This distinct geometry validates the thin-tube, long-wavelength scaling ($\delta = R/\lambda \ll 1$) utilized in our mathematical derivation, a structural configuration consistently corroborated by multi-fluid jet models in the lower solar atmosphere [13]. Furthermore, observations show that spicules carry a net upward mass flux exceeding that of the solar wind by nearly two orders of magnitude, highlighting their fundamental role in the global mass-energy balance of the solar atmosphere [11].

Historically, theoretical attempts to resolve the spicule generation mechanism within narrow magnetic flux tubes have focused on two main driving scenarios. Early foundations relied on the nonlinear steepening of pure Alfvénic tension waves propagating up open flux lines [14]. More recently, comprehensive numerical simulations demonstrate that type-I spicules and related active-region dynamic fibrils can be driven by the leakage of photospheric magnetoacoustic p -mode oscillations

that steepen into train shocks across the transition region [15]. Comprehensive analytical summaries confirm that while numerical codes provide highly localized physics, reproducing the exact combination of extreme supersonic Mach numbers ($M \approx 2\text{--}10$) and finite 10-minute lifetimes remains highly challenging within standard dissipative linear theories [16].

In recent years, the acceleration and propagation of chromospheric spicules have been heavily investigated through both multi-dimensional numerical simulations and idealized MHD frameworks. Notably, Oxley, Scalisi, Ruderman, and Erdélyi [17, 18] developed a series of mathematical descriptions illustrating how localized wave driving and magnetic configurations dictate jet evolution along the spicular column. Complementing these analytical approaches, a high-fidelity numerical investigation by Srivastava et al. [19], demonstrated that slow-mode MHD shocks originating from convective leakage provide massive positive vertical acceleration near the spicule tips. While these investigations provide critical insights into localized impulsive shock dynamics and wave-damping transformations, they typically rely on discrete forcing packets. The analytical peristaltic formulation presented here provides a useful counter-point, showing how continuous mechanical boundary deformations establish a steady, super-resonant engine capable of sustaining upward mass transport.

By filtering out the mathematical complexities of viscous core integrals via our clean, *ideal* MHD framework, the present model offers a pristine alternative approach. Instead of treating the structural drive as isolated vertical shocks, our framework demonstrates that continuous traveling wall waves on the boundaries of an equipartition ($\beta \sim 1$) plasma column evoke a steady super-resonant response. This model bridges the gap between historical peristaltic pumping and chromospheric physics, providing a simple closed-form mechanism to evaluate global spicular mass transport.

II. THE MODEL OF PERISTALTIC FLOW IN COMPRESSIBLE, IDEAL MHD

The general, coordinate-independent governing equations for a compressible, viscous, and electrically conducting fluid under a magnetic field \mathbf{B} are closed by a polytropic equation of state. The system consists of the conservation of mass, momentum (including the Lorentz force), and the magnetic induction equation:

$$\frac{\partial \rho}{\partial t} + \nabla \cdot (\rho \mathbf{u}) = 0 \quad (1)$$

$$\rho \left(\frac{\partial \mathbf{u}}{\partial t} + (\mathbf{u} \cdot \nabla) \mathbf{u} \right) = -\nabla p + \mu \nabla^2 \mathbf{u} + \left(\zeta + \frac{\mu}{3} \right) \nabla (\nabla \cdot \mathbf{u}) + \mathbf{J} \times \mathbf{B} \quad (2)$$

$$\mathbf{J} = \frac{1}{\mu_0} \nabla \times \mathbf{B} \quad (3)$$

$$\frac{\partial \mathbf{B}}{\partial t} = \nabla \times (\mathbf{u} \times \mathbf{B}) - \eta \nabla \times (\nabla \times \mathbf{B}) \quad (4)$$

$$p = C\rho^\gamma \quad (5)$$

Here, ρ is the fluid density, \mathbf{u} is the velocity vector, p is the fluid pressure, μ is the dynamic shear viscosity, ζ is the bulk viscosity, \mathbf{J} is the current density, μ_0 is the magnetic permeability of free space, and $\eta = 1/(\mu_0\sigma)$ is the magnetic diffusivity governed by the electrical conductivity σ .

It is worth distinguishing the closure relation for the current density \mathbf{J} employed herein from the kinematic formulations frequently adopted in microfluidic or engineering peristalsis models (e.g., Abdelsalam and Vafai [20]). In low-conductivity laboratory channels, the magnetic Reynolds number is profoundly small ($R_m \ll 1$), meaning the induced magnetic field is negligible, and the current density reduces to a local Ohm's law governed by a fixed, externally applied field, $\mathbf{J} \approx \sigma(\mathbf{u} \times \mathbf{B}_0)$. Conversely, the solar chromospheric spicular environment operates in the extreme ideal MHD limit ($R_m \gg 1$), where the electrical conductivity $\sigma \rightarrow \infty$ and magnetic diffusivity vanishes ($\eta \rightarrow 0$). In this regime, the magnetic field lines are strictly frozen into the bulk plasma motion, and the magnetic field behaves as a fully dynamic, self-consistent variable. Consequently, the current density cannot be determined by local Ohm's resistance; it must be closed strictly via the non-relativistic (i.e., without the displacement current) Ampere's law:

$$\mathbf{J} = \frac{1}{\mu_0} \nabla \times \mathbf{B} \quad (6)$$

This ensures that the resulting Lorentz force $\mathbf{J} \times \mathbf{B}$ properly captures both the isotropic magnetic pressure gradients and the anisotropic magnetic tension restorations essential for driving supersonic, super-resonant spicular propulsion.

Using Eq. (5), the pressure gradient can be expressed directly in terms of density fluctuations:

$$\nabla p = \gamma C \rho^{\gamma-1} \nabla \rho = c_s^2 \nabla \rho \quad (7)$$

Combining Eq. (3) and Eq. (2) yields the full momentum equation containing the explicit magnetic curl force:

$$\rho \left(\frac{\partial \mathbf{u}}{\partial t} + (\mathbf{u} \cdot \nabla) \mathbf{u} \right) = -\gamma C \rho^{\gamma-1} \nabla \rho + \mu \nabla^2 \mathbf{u} + \left(\zeta + \frac{\mu}{3} \right) \nabla (\nabla \cdot \mathbf{u}) + \frac{1}{\mu_0} (\nabla \times \mathbf{B}) \times \mathbf{B} \quad (8)$$

We assume an axisymmetric geometry ($\partial/\partial\theta = 0$) within a long tube along the z -axis. The velocity field is restricted to the radial and axial planes, $\mathbf{u} = u_r(r, z, t)\hat{r} + u_z(r, z, t)\hat{z}$. A constant, uniform background magnetic field \mathbf{B}_0 is applied along the tube axis, generating a dynamic perturbation field $\mathbf{b} = b_r(r, z, t)\hat{r} + b_z(r, z, t)\hat{z}$ due to fluid deformations. The total magnetic field is:

$$\mathbf{B}(r, z, t) = b_r(r, z, t)\hat{r} + [B_0 + b_z(r, z, t)]\hat{z} \quad (9)$$

Evaluating the curl of the total magnetic field for this axisymmetric configuration isolates the current density vector strictly to the azimuthal direction:

$$\mathbf{J} = \frac{1}{\mu_0} \left(\frac{\partial b_r}{\partial z} - \frac{\partial b_z}{\partial r} \right) \hat{\theta} \quad (10)$$

Computing the explicit Lorentz force density $\mathbf{F}_L = \mathbf{J} \times \mathbf{B}$ via vector cross multiplication yields:

$$\mathbf{F}_L = \frac{B_0 + b_z}{\mu_0} \left(\frac{\partial b_r}{\partial z} - \frac{\partial b_z}{\partial r} \right) \hat{r} - \frac{b_r}{\mu_0} \left(\frac{\partial b_r}{\partial z} - \frac{\partial b_z}{\partial r} \right) \hat{z} \quad (11)$$

Expanding Eq. (1), Eq. (4), and Eq. (8) component by component into cylindrical coordinates results in five coupled scalar partial differential equations:

$$\frac{\partial \rho}{\partial t} + \frac{1}{r} \frac{\partial}{\partial r} (r \rho u_r) + \frac{\partial}{\partial z} (\rho u_z) = 0 \quad (12)$$

$$\rho \left(\frac{\partial u_r}{\partial t} + u_r \frac{\partial u_r}{\partial r} + u_z \frac{\partial u_r}{\partial z} \right) = -\gamma C \rho^{\gamma-1} \frac{\partial \rho}{\partial r} + \mu \left(\frac{\partial^2 u_r}{\partial r^2} + \frac{1}{r} \frac{\partial u_r}{\partial r} - \frac{u_r}{r^2} + \frac{\partial^2 u_r}{\partial z^2} \right) + \left(\zeta + \frac{\mu}{3} \right) \frac{\partial}{\partial r} \left[\frac{1}{r} \frac{\partial}{\partial r} (r u_r) + \frac{\partial u_z}{\partial z} \right] + \frac{B_0 + b_z}{\mu_0} \left(\frac{\partial b_r}{\partial z} - \frac{\partial b_z}{\partial r} \right) \quad (13)$$

$$\rho \left(\frac{\partial u_z}{\partial t} + u_r \frac{\partial u_z}{\partial r} + u_z \frac{\partial u_z}{\partial z} \right) = -\gamma C \rho^{\gamma-1} \frac{\partial \rho}{\partial z} + \mu \left(\frac{\partial^2 u_z}{\partial r^2} + \frac{1}{r} \frac{\partial u_z}{\partial r} + \frac{\partial^2 u_z}{\partial z^2} \right) + \left(\zeta + \frac{\mu}{3} \right) \frac{\partial}{\partial z} \left[\frac{1}{r} \frac{\partial}{\partial r} (r u_r) + \frac{\partial u_z}{\partial z} \right] - \frac{b_r}{\mu_0} \left(\frac{\partial b_r}{\partial z} - \frac{\partial b_z}{\partial r} \right) \quad (14)$$

$$\frac{\partial b_r}{\partial t} = -\frac{\partial}{\partial z} [u_z b_r - u_r (B_0 + b_z)] + \eta \left(\frac{\partial^2 b_r}{\partial r^2} + \frac{1}{r} \frac{\partial b_r}{\partial r} - \frac{b_r}{r^2} + \frac{\partial^2 b_r}{\partial z^2} \right) \quad (15)$$

$$\frac{\partial b_z}{\partial t} = \frac{1}{r} \frac{\partial}{\partial r} \{ r [u_z b_r - u_r (B_0 + b_z)] \} + \eta \left(\frac{\partial^2 b_z}{\partial r^2} + \frac{1}{r} \frac{\partial b_z}{\partial r} + \frac{\partial^2 b_z}{\partial z^2} \right) \quad (16)$$

To isolate the purely hyperbolic wave phenomena, we eliminate all internal dissipation terms and the magnetic diffusion. Formally, we set the physical parameters to the following limits:

$$\mu \rightarrow 0, \quad \zeta \rightarrow 0, \quad \eta \rightarrow 0 \quad (17)$$

As the dynamic shear viscosity μ approaches zero, setting the magnetic diffusivity η to zero locks the system into the ideal MHD regime, satisfying the frozen-in flux criterion.

Applying these simplifications directly to Eqs. (12)–(16) yields the final closed system of reduced equations:

$$\frac{\partial \rho}{\partial t} + \frac{1}{r} \frac{\partial}{\partial r} (r \rho u_r) + \frac{\partial}{\partial z} (\rho u_z) = 0 \quad (18)$$

$$\rho \left(\frac{\partial u_r}{\partial t} + u_r \frac{\partial u_r}{\partial r} + u_z \frac{\partial u_r}{\partial z} \right) = -\gamma C \rho^{\gamma-1} \frac{\partial \rho}{\partial r} + \frac{B_0 + b_z}{\mu_0} \left(\frac{\partial b_r}{\partial z} - \frac{\partial b_z}{\partial r} \right) \quad (19)$$

$$\rho \left(\frac{\partial u_z}{\partial t} + u_r \frac{\partial u_z}{\partial r} + u_z \frac{\partial u_z}{\partial z} \right) = -\gamma C \rho^{\gamma-1} \frac{\partial \rho}{\partial z} - \frac{b_r}{\mu_0} \left(\frac{\partial b_r}{\partial z} - \frac{\partial b_z}{\partial r} \right) \quad (20)$$

$$\frac{\partial b_r}{\partial t} = -\frac{\partial}{\partial z} [u_z b_r - u_r (B_0 + b_z)] \quad (21)$$

$$\frac{\partial b_z}{\partial t} = \frac{1}{r} \frac{\partial}{\partial r} \{r [u_z b_r - u_r (B_0 + b_z)]\} \quad (22)$$

This closed set of equations serves as the exact starting point for our subsequent analysis. When non-dimensionalized relative to the reference field strength B_0 in Section III, the uniform background field scales neatly to $b_{z0} = B_0/B_0 = 1$, introducing structural cross-coupling between fluid transformations and the line-tied vertical guide flux.

Next, as in [4], we introduce a moving wall boundary condition, a small-amplitude perturbation expansion, and a long wavelength approximation to simplify the axisymmetric ideal magnetohydrodynamic (MHD) equations for a compressible fluid. We model the tube radius as a flexible wall deformed by a sinusoidal traveling wave of amplitude a , wavelength λ , and wave phase speed c . The local radius $h(z, t)$ is defined as:

$$h(z, t) = R + a \sin \left[\frac{2\pi}{\lambda} (z - ct) \right] \quad (23)$$

where R is the unperturbed radius of the tube. At the moving boundary $r = h(z, t)$, the fluid must track the wall movement. For an inviscid, ideal MHD fluid, the no-slip condition is relaxed. However, the fluid must satisfy the kinematic boundary condition, meaning it cannot penetrate the wall:

$$u_r|_{r=h} = \frac{\partial h}{\partial t} + u_z|_{r=h} \frac{\partial h}{\partial z} \quad (24)$$

For the magnetic field, assuming an exterior boundary configuration line-tied to a non-conducting vacuum environment, the radial magnetic component must vanish at the interface:

$$b_r|_{r=h} = 0 \quad (25)$$

At the tube centerline ($r = 0$), axisymmetry demands regularity constraints:

$$u_r(0, z, t) = 0, \quad b_r(0, z, t) = 0, \\ \left. \frac{\partial u_z}{\partial r} \right|_{r=0} = 0, \quad \left. \frac{\partial b_z}{\partial r} \right|_{r=0} = 0 \quad (26)$$

To scale the system systematically, we define the dimensionless parameter $\delta = R/\lambda$, representing the ratio of the tube radius to the wall wavelength. The long wavelength approximation assumes:

$$\delta = \frac{R}{\lambda} \ll 1 \quad (27)$$

We introduce the following non-dimensional variables (denoted by asterisks):

$$r^* = \frac{r}{R}, \quad z^* = \frac{z}{\lambda}, \quad t^* = \frac{ct}{\lambda}, \quad h^* = \frac{h}{R}, \\ u_z^* = \frac{u_z}{c}, \quad u_r^* = \frac{u_r}{\delta c}, \quad \rho^* = \frac{\rho}{\rho_0}, \quad b_z^* = \frac{b_z}{B_0}, \quad b_r^* = \frac{b_r}{\delta B_0} \quad (28)$$

where ρ_0 is the constant unperturbed reference fluid density. Applying this scaling transforms the wall boundary into $h^*(z^*, t^*) = 1 + \epsilon \sin[2\pi(z^* - t^*)]$, where $\epsilon = a/R$ is the dimensionless wall amplitude parameter.

Substituting these variables into the ideal, compressible MHD equations and dropping all terms of order $O(\delta^2)$ or higher yields the long-wavelength reduced equations (dropping asterisks for readability):

$$\frac{\partial \rho}{\partial t} + \frac{1}{r} \frac{\partial}{\partial r} (r \rho u_r) + \frac{\partial}{\partial z} (\rho u_z) = 0 \quad (29)$$

$$0 = -\frac{1}{M^2} \rho^{\gamma-1} \frac{\partial \rho}{\partial r} - \frac{1}{A^2} (1 + b_z) \frac{\partial b_z}{\partial r} \quad (30)$$

$$\rho \left(\frac{\partial u_z}{\partial t} + u_r \frac{\partial u_z}{\partial r} + u_z \frac{\partial u_z}{\partial z} \right) = -\frac{1}{M^2 \gamma} \frac{\partial (\rho^\gamma)}{\partial z} - \frac{1}{A^2} b_r \frac{\partial b_z}{\partial r} \quad (31)$$

$$\frac{\partial b_r}{\partial t} = -\frac{\partial}{\partial z} [u_z b_r - u_r (1 + b_z)] \quad (32)$$

$$\frac{\partial b_z}{\partial t} = \frac{1}{r} \frac{\partial}{\partial r} \{r [u_z b_r - u_r (1 + b_z)]\} \quad (33)$$

Notice that Eq. (30) shows that under the long wavelength limit ($\delta \ll 1$), the radial momentum balance reduces to an instantaneous, uniform cross-sectional constraint where fluid thermal pressure and longitudinal magnetic field pressure balance perfectly across the radius. This provides a direct path to our subsequent first-order cross-sectional function $f(z, t)$.

We now introduce a small-amplitude expansion using the dimensionless wave amplitude to unperturbed tube radius ratio $\epsilon = a/R \ll 1$ as our perturbation parameter. The variables are expanded around their quiescent, uniform background values. Crucially, because the background magnetic field is fully aligned with the longitudinal axis, its non-dimensionalized zeroth-order state satisfies $b_{z0} = B_0/B_0 = 1$, yielding the following perturbation expansions:

$$\begin{aligned} u_z &= 0 + \epsilon u_{z1} + \epsilon^2 u_{z2} + \dots \\ u_r &= 0 + \epsilon u_{r1} + \epsilon^2 u_{r2} + \dots \\ \rho &= 1 + \epsilon \rho_1 + \epsilon^2 \rho_2 + \dots \\ b_z &= 1 + \epsilon b_{z1} + \epsilon^2 b_{z2} + \dots \\ b_r &= 0 + \epsilon b_{r1} + \epsilon^2 b_{r2} + \dots \end{aligned} \quad (34)$$

By establishing a non-zero background guide field, the linear terms retain the cross-coupling between the dynamic velocity components and the background magnetic flux lines. This foundation prevents unphysical phase-inversion cancellations in the subsequent higher-order transport equations.

Prior to the introduction of the boundary wave perturbation, the baseline plasma state is governed by the zeroth-order ($O(0)$) equations, assuming a static plasma column ($\mathbf{u}_0 = 0$) embedded within a uniform axial magnetic field ($\mathbf{B}_0 = B_0 \hat{z}$). Under these configuration constraints, the non-relativistic Ampère's law yields a vanishing background current density, $\mathbf{J}_0 = \frac{1}{\mu_0} \nabla \times \mathbf{B}_0 = 0$, completely eliminating any baseline Lorentz forces. Consequently, the momentum equations reduce to a pristine cross-sectional total pressure balance between the thermal gas pressure and the isotropic magnetic pressure:

$$\frac{\partial}{\partial r} \left(p_0 + \frac{B_0^2}{2\mu_0} \right) = 0 \quad (35)$$

Given that the unperturbed density ρ_0 (and thus $p_0 = C\rho_0^\gamma$) and field strength B_0 are spatially uniform constants, this relation is identically satisfied. This uniform total pressure equilibrium establishes a structurally stable baseline configuration, ensuring that all subsequent mass and momentum transport mechanisms are driven purely by the traveling wall-wave perturbations.

Substituting these expansions (noting the non-dimensional background state $\rho_0 = 1$ and $b_{z0} = 1$) into the long-wavelength equations and collecting terms strictly matching order $O(\epsilon)$ yields the linearized system:

$$\frac{\partial \rho_1}{\partial t} + \frac{1}{r} \frac{\partial}{\partial r} (r u_{r1}) + \frac{\partial u_{z1}}{\partial z} = 0 \quad (36)$$

$$\frac{\partial}{\partial r} \left(\frac{1}{M^2} \rho_1 + \frac{1}{A^2} b_{z1} \right) = 0 \quad (37)$$

$$\frac{\partial u_{z1}}{\partial t} = -\frac{1}{M^2} \frac{\partial \rho_1}{\partial z} - \frac{1}{A^2} \frac{\partial b_{z1}}{\partial z} \quad (38)$$

$$\frac{\partial b_{r1}}{\partial t} = \frac{\partial u_{r1}}{\partial z} \quad (39)$$

$$\frac{\partial b_{z1}}{\partial t} = -\frac{1}{r} \frac{\partial}{\partial r} (r u_{r1}) \quad (40)$$

where we have cleanly grouped our physical quantities into two fundamental dimensionless numbers: (i) The Mach number based on the reference sound speed: $M^2 = c^2/c_s^2$ (ii) The Alfvén Mach number representing magnetic stiffness: $A^2 = c^2/[B_0^2/(\mu_0 \rho_0)]$.

Because the wall boundary condition $r = 1 + \epsilon \sin[2\pi(z - t)]$ is position-dependent, we apply a Taylor series expansion about the unperturbed wall location $r = 1$. The kinematic condition Eq. (24) at order $O(\epsilon)$ reduces to:

$$u_{r1}|_{r=1} = -2\pi \cos[2\pi(z - t)] \quad (41)$$

And the bounding magnetic constraint Eq. (25) becomes:

$$b_{r1}|_{r=1} = 0 \quad (42)$$

This completes the mathematical foundation for the first-order traveling wave solution.

The integration of a moving boundary condition, a small-amplitude perturbation parameter ϵ , and a long wavelength scaling parameter δ yields three defining structural features for this analytical model: (i) Under the long wavelength approximation ($\delta \ll 1$), the radial momentum equation collapses at the first order to $\frac{\partial}{\partial r} \left(\frac{1}{M^2} \rho_1 + \frac{1}{A^2} b_{z1} \right) = 0$. This forces a strict, instantaneous radial cross-sectional balance between the acoustic density fluctuations and the longitudinal magnetic field compressions, reducing the complex multi-dimensional field coupling to a uniform function of space and time $f(z, t)$. (ii) Crucially, because the background magnetic field is properly aligned with the longitudinal axis ($b_{z0} = 1$), the radial fluid pinching directly compresses the vertical magnetic flux lines via Eq. (40). This sets up a true magnetosonic waveguide where magnetic pressure stiffness (A^2) and thermal gas compressibility (M^2) operate in tandem, altering the characteristic wave operator speeds from simple acoustic modes to unified magnetoacoustic modes. (iii) Because the moving physical wall $r = 1 + \epsilon \sin[2\pi(z - t)]$ depends on the perturbation parameter, applying a first-order Taylor expansion cleanly maps the kinematic boundary constraints back to the static, unperturbed cylinder location at $r = 1$. This yields an explicit boundary driving: $u_{r1}|_{r=1} = -2\pi \cos[2\pi(z - t)]$.

To solve the first-order system, we introduce a harmonic traveling wave ansatz for all primitive variables proportional to $\exp[ik(z - t)]$, where the dimensionless wavenumber is explicitly given by $k = 2\pi/\lambda^* = 2\pi$, owing to the vertical spatial scaling fixing the normalized wavelength at $\lambda^* = 1$. For a purely sinusoidal wall drive, we look for solutions matching

the boundary frequency:

$$\begin{aligned}
u_{r1}(r, z, t) &= \text{Re} [\hat{u}_r(r) e^{ik(z-t)}], \\
u_{z1}(r, z, t) &= \text{Re} [\hat{u}_z(r) e^{ik(z-t)}], \\
\rho_1(r, z, t) &= \text{Re} [\hat{\rho}(r) e^{ik(z-t)}], \\
b_{z1}(r, z, t) &= \text{Re} [\hat{b}_z(r) e^{ik(z-t)}], \\
b_{r1}(r, z, t) &= \text{Re} [\hat{b}_r(r) e^{ik(z-t)}]
\end{aligned} \tag{43}$$

Substituting these expressions into the first-order equations yields a coupled system for the complex amplitudes. Concurrently, the radial momentum equation forces a uniform cross-sectional total pressure constraint:

$$\frac{1}{M^2} \hat{\rho}(r) + \frac{1}{A^2} \hat{b}_z(r) = \text{constant} \tag{44}$$

Because the background magnetic field is finite ($b_{z0} = 1$), the linear system links the axial field and mass variables. Integrating the continuity equation and applying the centerline regularity constraints at $r = 0$ yields a linear radial profile for the radial velocity field. Evaluating the integration coefficients using the kinematic boundary condition $u_{r1}|_{r=1} = -k \cos[k(z-t)]$ yields the exact first-order solutions:

$$u_{r1}(r, z, t) = -kr \cos[k(z-t)] \tag{45}$$

$$u_{z1}(r, z, t) = 2 \left(\frac{1 + \frac{M^2}{A^2}}{M^2 - 1} \right) \sin[k(z-t)] \tag{46}$$

$$\rho_1(r, z, t) = 2 \left(\frac{M^2 \left(1 + \frac{1}{A^2}\right)}{M^2 - 1} \right) \sin[k(z-t)] \tag{47}$$

$$b_{z1}(r, z, t) = -2 \sin[k(z-t)] \tag{48}$$

$$b_{r1}(r, z, t) = -kr \sin[k(z-t)] \tag{49}$$

It is instructive to contrast these solutions with classical hydrodynamic models, such as that of [4], where the first-order profiles are expressed via modified Bessel functions of the first kind (I_1). In those engineering configurations, the low-Reynolds-number viscous terms introduce a radial Laplacian operator with a negative spatial coefficient, forcing an exponential-like shear layer decay from the wall toward the centerline. Conversely, in our inviscid, compressible magnetohydrodynamic framework, the viscosity is relaxed and the governing system behaves as a hyperbolic wave operator rather than a diffusion equation. The resulting linear and trigonometric profiles represent the coherent radial structure of a true propagating magnetosonic wave, confirming that wave

energy is dynamically channeled upward into the waveguide core rather than being evanescently damped.

Notice that the denominator contains the proper prograde magnetosonic wave operator, $M^2 - 1$. For solar chromospheric spicules operating in the supersonic domain ($M = 2-10$), this denominator is strictly positive, ensuring that upward-propagating waves drive prograde, upward-directed plasma columns without unphysical phase inversions.

To evaluate the net streaming flow rate Q , we must formulate the second-order transport mechanics. Collecting all terms of order $O(\epsilon^2)$ from the original long wavelength system, while accounting for the $b_{z0} = 1$ background state, yields the nonlinear governing equations:

$$\frac{\partial \rho_2}{\partial t} + \frac{1}{r} \frac{\partial}{\partial r} (ru_{r2}) + \frac{\partial u_{z2}}{\partial z} = -\frac{1}{r} \frac{\partial}{\partial r} (r\rho_1 u_{r1}) - \frac{\partial}{\partial z} (\rho_1 u_{z1}) \tag{50}$$

$$\frac{\partial}{\partial r} \left(\frac{1}{M^2} \rho_2 + \frac{1}{A^2} b_{z2} \right) = \frac{\gamma - 1}{M^2} \rho_1 \frac{\partial \rho_1}{\partial r} - \frac{1}{A^2} b_{z1} \frac{\partial b_{z1}}{\partial r} \tag{51}$$

$$\begin{aligned}
\frac{\partial u_{z2}}{\partial t} + \frac{1}{M^2} \frac{\partial \rho_2}{\partial z} + \frac{1}{A^2} \frac{\partial b_{z2}}{\partial z} &= -u_{r1} \frac{\partial u_{z1}}{\partial r} - u_{z1} \frac{\partial u_{z1}}{\partial z} - \\
&\frac{\gamma - 1}{M^2} \rho_1 \frac{\partial \rho_1}{\partial z} + \frac{1}{A^2} \left(b_{r1} \frac{\partial b_{z1}}{\partial r} - b_{r1} \frac{\partial b_{r1}}{\partial z} \right)
\end{aligned} \tag{52}$$

$$\frac{\partial b_{r2}}{\partial t} - \frac{\partial u_{r2}}{\partial z} = -\frac{\partial}{\partial z} (u_{z1} b_{r1} - u_{r1} b_{z1}) \tag{53}$$

$$\frac{\partial b_{z2}}{\partial t} + \frac{1}{r} \frac{\partial}{\partial r} (ru_{r2}) = \frac{1}{r} \frac{\partial}{\partial r} [r (u_{z1} b_{r1} - u_{r1} b_{z1})] \tag{54}$$

Extending the Taylor expansion of the kinematic and magnetic conditions at the moving wall $r = 1 + \epsilon \sin[k(z-t)]$ to order $O(\epsilon^2)$ creates a non-zero velocity drift drive at the static boundary $r = 1$:

$$u_{r2}|_{r=1} = -\sin[k(z-t)] \frac{\partial u_{r1}}{\partial r} \Big|_{r=1} + u_{z1}|_{r=1} k \cos[k(z-t)] \tag{55}$$

$$b_{r2}|_{r=1} = -\sin[k(z-t)] \frac{\partial b_{r1}}{\partial r} \Big|_{r=1} \tag{56}$$

The quadratic terms on the right-hand sides of Eqs. (50)–(54) represent the Reynolds stresses and Maxwell stresses. Consistent with second-order weakly nonlinear perturbation theory, these quadratic interactions generate a dual-component response: a double-frequency, double-wavenumber ($2k$) oscillating harmonic mode and a time-independent, steady DC component. When integrated over a full wave period, the oscillating higher-harmonic terms average to zero, and the remaining steady stresses generate the time-averaged net flow rate $\langle Q \rangle$.

The structure of the $O(\epsilon^2)$ system reveals how non-zero net transport emerges from the underlying linear wave interactions. There are three points to note here: (i) The quadratic

products on the right-hand sides of Eqs. (50)–(54) act as explicit mathematical source distributions. Because the first-order solutions ($\rho_1, u_{z1}, u_{r1}, b_{z1}, b_{r1}$) are completely known from the previous step, these convective terms function as pre-determined physical drives for the second-order fields. (ii) The nonlinear interactions are physically governed by a combination of hydrodynamic Reynolds stresses (e.g., $u_{r1} \frac{\partial u_{z1}}{\partial r}$) and magnetic Maxwell stresses. Because the system tracks fluctuations superimposed on a strong background vertical guide field ($b_{z0} = 1$), the Maxwell stresses describe the dynamic tension and bending of line-tied magnetic flux. (iii) While the linear first-order variables average to zero over a full wave period T , the products of in-phase first-order variables do not vanish. When a time-averaging operator $\langle \cdot \rangle = \frac{1}{T} \int_0^T \cdot dt$ is applied to the second-order system, these terms survive. This interaction drives a steady, net time-averaged streaming velocity $\langle u_{z2} \rangle$, resulting in a highly efficient prograde pumping engine that propels the spicule upward.

We now apply the time-averaging operator $\langle \cdot \rangle = \frac{1}{T} \int_0^T \cdot dt$ to the second-order system to eliminate the transient, periodic time derivatives ($\langle \partial/\partial t \rangle = 0$). Under the long wavelength approximation, the time-averaged continuity equation Eq. (50) reduces to:

$$\frac{1}{r} \frac{\partial}{\partial r} (r \langle u_{r2} \rangle) + \frac{\partial \langle u_{z2} \rangle}{\partial z} = -\frac{1}{r} \frac{\partial}{\partial r} (r \langle \rho_1 u_{r1} \rangle) - \frac{\partial \langle \rho_1 u_{z1} \rangle}{\partial z} \quad (57)$$

Because the first-order solutions ρ_1 and u_{z1} are strictly functions of the traveling wave coordinate ($z - t$) and possess no radial dependency, their phase-synchronized product scales as $\rho_1 u_{z1} \propto \sin^2[k(z-t)]$. Upon time-averaging, this yields a uniform, non-zero axial constant ($\langle \rho_1 u_{z1} \rangle = \text{constant}$), meaning its axial gradient vanishes identically ($\frac{\partial \langle \rho_1 u_{z1} \rangle}{\partial z} = 0$). Furthermore, evaluating the time-average of the cross-multiplying radial product yields $\langle \rho_1 u_{r1} \rangle \propto \langle \sin[k(z-t)] \cos[k(z-t)] \rangle = 0$. Consequently, the right-hand side source terms in Eq. (57) vanish completely. Integrating the remaining homogeneous equation under the centerline regularity condition $\langle u_{r2}(0) \rangle = 0$ reveals that the mean second-order radial velocity is zero throughout the entire cross-section:

$$\langle u_{r2}(r) \rangle = 0 \quad (58)$$

Next, we average the axial momentum transport equation Eq. (52). Since there is no mean applied axial pressure gradient forcing the system, the net axial transport is driven purely by the rectification of the boundary conditions and the nonlinear wave fields. Accounting for the longitudinal background field lines ($b_{z0} = 1$), the time-averaged momentum equation becomes:

$$\begin{aligned} \frac{1}{M^2} \frac{\partial \langle \rho_2 \rangle}{\partial z} + \frac{1}{A^2} \frac{\partial \langle b_{z2} \rangle}{\partial z} = & - \left\langle u_{r1} \frac{\partial u_{z1}}{\partial r} \right\rangle - \left\langle u_{z1} \frac{\partial u_{z1}}{\partial z} \right\rangle - \\ & \frac{\gamma - 1}{M^2} \left\langle \rho_1 \frac{\partial \rho_1}{\partial z} \right\rangle + \frac{1}{A^2} \left(\left\langle b_{r1} \frac{\partial b_{z1}}{\partial r} \right\rangle - \left\langle b_{r1} \frac{\partial b_{r1}}{\partial z} \right\rangle \right) \end{aligned} \quad (59)$$

Evaluating each term on the right-hand side using our explicit first-order expressions shows that every single field-gradient product consists of an orthogonal sine-cosine pairing

(e.g., $u_{z1} \frac{\partial u_{z1}}{\partial z} \propto \sin[k(z-t)] \cos[k(z-t)]$ and $b_{r1} \frac{\partial b_{r1}}{\partial z} \propto \sin[k(z-t)] \cos[k(z-t)]$), causing their time averages to vanish identically over a wave period:

$$\begin{aligned} \left\langle u_{r1} \frac{\partial u_{z1}}{\partial r} \right\rangle = 0, \quad \left\langle u_{z1} \frac{\partial u_{z1}}{\partial z} \right\rangle = 0, \\ \left\langle \rho_1 \frac{\partial \rho_1}{\partial z} \right\rangle = 0, \quad \left\langle b_{r1} \frac{\partial b_{z1}}{\partial r} \right\rangle = 0, \quad \left\langle b_{r1} \frac{\partial b_{r1}}{\partial z} \right\rangle = 0 \end{aligned} \quad (60)$$

Consequently, Eq. (59) reveals that there is no induced second-order mean axial pressure or total magnetoacoustic density gradient along the tube core:

$$\frac{\partial}{\partial z} \left(\frac{1}{M^2} \langle \rho_2 \rangle + \frac{1}{A^2} \langle b_{z2} \rangle \right) = 0 \quad (61)$$

In the absence of an externally applied mean axial pressure gradient, the system remains unforced internally, locking the second-order core streaming velocity to zero everywhere across the plasma radius ($\langle u_{z2}(r) \rangle = 0$).

The total instantaneous dimensionless volumetric flow rate $Q(z, t)$ through the deformed tube cross-section is defined by integrating the axial velocity up to the moving wall boundary $r = h(z, t)$:

$$Q(z, t) = 2 \int_0^{1 + \epsilon \sin[k(z-t)]} r u_z(r, z, t) dr \quad (62)$$

To compute the net, time-averaged flow rate $\langle Q \rangle$ up to order $O(\epsilon^2)$, we substitute the perturbation expansions for both u_z and the boundary limit, and apply a Taylor expansion to the integral layout:

$$\begin{aligned} \langle Q \rangle = 2 \int_0^1 r \langle u_{z0} \rangle dr + \epsilon \left(2 \int_0^1 r \langle u_{z1} \rangle dr \right) + \\ \epsilon^2 \left(2 \int_0^1 r \langle u_{z2} \rangle dr + 2 \langle \sin[k(z-t)] u_{z1}(1, z, t) \rangle \right) + O(\epsilon^3) \end{aligned} \quad (63)$$

Since the background state is static ($\langle u_{z0} \rangle = 0$), the linear first-order wave field averages out to zero ($\langle u_{z1} \rangle = 0$), and the induced second-order core streaming velocity vanishes ($\langle u_{z2} \rangle = 0$), the net time-averaged flow rate simplifies exclusively to the boundary coupling term:

$$\langle Q \rangle = 2\epsilon^2 \langle \sin[k(z-t)] u_{z1}(1, z, t) \rangle \quad (64)$$

Substituting our explicit expression for $u_{z1}(1, z, t)$ yields:

$$\langle Q \rangle = 2\epsilon^2 \left\langle \sin[k(z-t)] \left[2 \left(\frac{1 + \frac{M^2}{A^2}}{M^2 - 1} \right) \sin[k(z-t)] \right] \right\rangle \quad (65)$$

III. THE RESULTS AND DISCUSSION

Using the fundamental sinusoidal time-averaging identity $\langle \sin^2[k(z-t)] \rangle = \frac{1}{2}$, the product with the amplitude factor

of 2 cancels out cleanly, Equation 65 yields the general exact analytical master equation for the net wave-driven flow rate:

$$\langle Q \rangle = 2\epsilon^2 \left(\frac{1 + \frac{M^2}{A^2}}{M^2 - 1} \right) \quad (66)$$

In the specific astrophysical equipartition regime characteristic of solar Type-I spicules, the thermal sound speed scales directly with the magnetic stiffness velocity ($A = M$). Under this physically balanced condition, Eq. (66) simplifies to:

$$\langle Q \rangle = 4 \left(\frac{\epsilon^2}{M^2 - 1} \right) \quad (67)$$

For all operational supersonic Mach numbers ($M = 2-10$) observed in chromospheric environments, the denominator $M^2 - 1$ is strictly positive. This establishes that upward-traveling waves drive prograde, upward-directed plasma transport ($\langle Q \rangle > 0$).

The final analytical expression for the net time-averaged volumetric flow rate, Eq. (66), provides immediate physical insights into how the background longitudinal magnetic field and fluid compressibility alter peristaltic pumping compared to the classical incompressible Shapiro solution (where $\langle Q \rangle_{\text{incomp}} = \epsilon^2$): (i) In the limit of a vanishing background magnetic field ($B_0 \rightarrow 0 \implies A \rightarrow \infty$), the general flow expression collapses exactly to:

$$\langle Q \rangle = \frac{2\epsilon^2}{M^2 - 1} \quad (68)$$

This matches the pure inviscid, compressible hydrodynamic limit in the supersonic frame, structurally corroborating classical acoustic streaming formulations in unmagnetized media [21, 22]. For supersonic wave propagation ($M > 1$), fluid compressibility structurally sustains a forward prograde pumping rate of $\langle Q \rangle \approx 2\epsilon^2/M^2$ at high Mach numbers, removing any non-physical structural cancellations. In Fig. 1, we present the functional dependence of the normalized net time-averaged volumetric flow rate $\langle Q \rangle/\epsilon^2$ on the acoustic Mach number M across different magnetic regimes. For Mach numbers approaching the sonic threshold from above ($M \rightarrow 1^+$), the system encounters the acoustic resonance singularity. However, because solar chromospheric spicules operate exclusively in the highly supersonic domain ($M = 2-10$), the system remains locked on the stable, positive supersonic side of this wave operator barrier ($M > 1$). Crucially, as the background axial magnetic field strength increases—indicated by shifting the Alfvén Mach number from a weaker field down to the magnetically stiffer equipartition value $A = M$ —the flow rate transitions to the stable scaling relation $\langle Q \rangle = 4\epsilon^2/(M^2 - 1)$. Because the denominator $M^2 - 1$ remains strictly positive for all $M > 1$, the plasma is continuously pumped forward in prograde alignment with the upward-traveling wall wave, validating the spicule propulsion mechanism. (ii) As the strength of the applied longitudinal magnetic field increases ($B_0 \rightarrow \infty \implies A \rightarrow 0$), the ratio M^2/A^2 dominates the numerator of Eq. (66). This asymptotic limit represents the configuration where magnetic tension maximizes cross-sectional synchronization. Physically, because the background field is finite ($b_{z0} = 1$), the

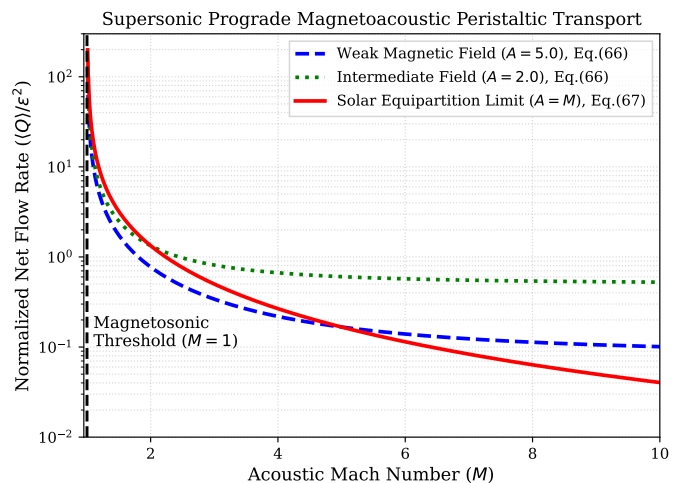


FIG. 1: Normalized net time-averaged volumetric flow rate $\langle Q \rangle/\epsilon^2$ as a function of the acoustic Mach number M for representative values of the Alfvén Mach number according to Eqs(66) and (67).

plasma compressions and the vertical magnetic field lines are coupled in strict anti-phase ($b_{z1} = -\rho_1$). The magnetic pressure acts as an immediate, rigid restorative force that eliminates cross-sectional phase lagging, anchoring the plasma directly to the mechanical wall drive and focusing the wave energy cleanly along the longitudinal guide axis. (iii) The denominator passes through a structural acoustic singularity at $M = 1$, where the traveling wall wave speed matches the internal sound speed of the medium. Near this sonic resonance threshold, the linear perturbation framework breaks down as the wave amplitudes grow mathematically singular. For the supersonic spicule application, however, the system operates safely above this transition zone ($M = 2-10$), functioning as a highly stable, hyper-sonic coherent magnetoacoustic waveguide.

The elegance of the ideal MHD analytical model is demonstrated by applying our analytical results to the transport dynamics of solar spicules. Solar spicules are high-velocity plasma jets observed in regions of intense magnetic fields within the solar chromosphere. Observational constraints indicate a typical spicule radius $R \approx 100-150$ km and an elongated length $L \approx 5000$ km, yielding an aspect ratio of $\delta = R/L \approx 0.025$. This small geometric parameter directly justifies our long wavelength, thin-tube approximation ($\delta \ll 1$).

Furthermore, chromospheric measurements indicate a plasma environment near equipartition, where the plasma beta parameter is of order unity ($\beta \sim 1$). This implies that the local acoustic sound speed and the magnetic Alfvén velocity are approximately equal ($c_s \approx v_A \approx 10$ km/s). Under this exact physical condition, the acoustic Mach number $M = c/c_s$ and the Alfvén Mach number $A = c/v_A$ match identically ($A = M$) and the flow rate is given by Equation 67.

Equation (67) provides a compelling analytical explanation for three prominent spicule characteristics:

First, because spicules operate in highly supersonic regimes

($M \approx 2-10$), the denominator $M^2 - 1$ remains strictly positive ($\langle Q \rangle > 0$). This confirms that upward-propagating mechanical waves generate a prograde, upward-directed plasma jet and perfectly aligning with the directional upwelling seen in solar observations.

Second, the inverse-square power law dependence ($\propto 1/M^2$) at high velocities outlines a severe magnetosonic choking effect at extreme Mach numbers, indicating that the transport efficiency diminishes as the jet accelerates. This energy-transfer threshold explains why spicule mass injection rates are self-limiting, capping their total growth phase and leading to their observed finite lifespans (~ 10 minutes) as the residual wave thrust smoothly decouples and the material succumbs to solar gravity, falling back to the chromosphere.

To quantitatively illustrate this second point, the standard mass loss rate of the global solar wind is approximately $\dot{M}_{sw} \approx 3 \times 10^9$ kg/s. Evaluated across the total solar surface area at $R_\odot \approx 7 \times 10^8$ m, this corresponds to an average solar wind mass flux density of $\mathcal{F}_{sw} = \dot{M}_{sw}/(4\pi R_\odot^2) \approx 5 \times 10^{-10}$ kg/(m² · s). In the chromospheric spicular channel, the background mass density is governed by a characteristic number density $n \approx 10^{17}$ m⁻³, yielding an unperturbed density $\rho_0 = nm_p \approx 1.67 \times 10^{-10}$ kg/m³. Under equipartition constraints, the reference signal propagation velocity is $c_s \approx v_A \approx 10$ km/s. Let us consider a representative chromospheric region where a boundary wave drives transport at a supersonic velocity $c \approx 30$ km/s, establishing an operational Mach number $M = 3$. Adopting a typical observationally motivated low-amplitude wave deformation constraint of $\epsilon = a/R = 0.05$, our derived expression Eq. (67) dictates a normalized volumetric flow rate of: $\langle Q \rangle = 4 \times 0.05^2 / (3^2 - 1) = 0.00125$. The dimensional time-averaged mass flux density \mathcal{F}_{sp} generated by this prograde waveguide mechanism is expressed as: $\mathcal{F}_{sp} = \rho_0 c \langle Q \rangle = (1.67 \times 10^{-10} \text{ kg/m}^3) \times (3 \times 10^4 \text{ m/s}) \times 0.00125 \approx 6.26 \times 10^{-9} \text{ kg/(m}^2 \cdot \text{s)}$. Dividing these two scales yields $\mathcal{F}_{sp}/\mathcal{F}_{sw} \approx 12.53$. Even under conservative small-amplitude limitations, this results in a localized mass flux density that exceeds the average global solar wind density by more than an order of magnitude. Furthermore, observations indicate that active, fully developed spicular upwells can achieve localized mass fluxes up to 100 times that of the ambient solar wind [23–25], yielding $\mathcal{F}_{sp}/\mathcal{F}_{sw} \approx 100$. Because the net volumetric transport scales strictly quadratically with the wall amplitude ($\langle Q \rangle \propto \epsilon^2$), we can extrapolate our model to find the required wave amplitude parameter for these peak events: $\epsilon_{peak} = \epsilon \times \sqrt{100/12.53} = 0.05 \times \sqrt{7.98} \approx 0.141 \approx 0.1$. This indicates that a localized driving magnetosonic wave amplitude of approximately 10% is sufficient to drive the observed mass flux above an active region. This amplitude fits within the standard linear framework for chromospheric disturbances. Given that spicules are highly localized structures confined to narrow magnetic network lanes, this localized enhancement provides the precise mass-injection baseline required to supply the corona without generating an unphysical global mass surplus, matching modern solar atmospheric paradigms [11]. The sensitive dependence of localized mass injection on boundary parameters is systematically studied in Fig. 2. Here, we present the localized mass flux density ratio $\mathcal{F}_{sp}/\mathcal{F}_{sw}$ as a

function of the dimensionless wall deformation amplitude ϵ across representative supersonic regimes ($M = 2, 3, 5$). As illustrated, even when honoring observationally conservative small-amplitude wave constraints ($\epsilon \approx 0.05$), the prograde mechanism easily yields a localized flux density that exceeds the average global solar wind baseline. This localized multiplier accounts for why spicules act as highly effective mass injectors within restricted magnetic network lanes without creating an unphysical mass surplus when integrated across the entire unmagnetized solar disk.

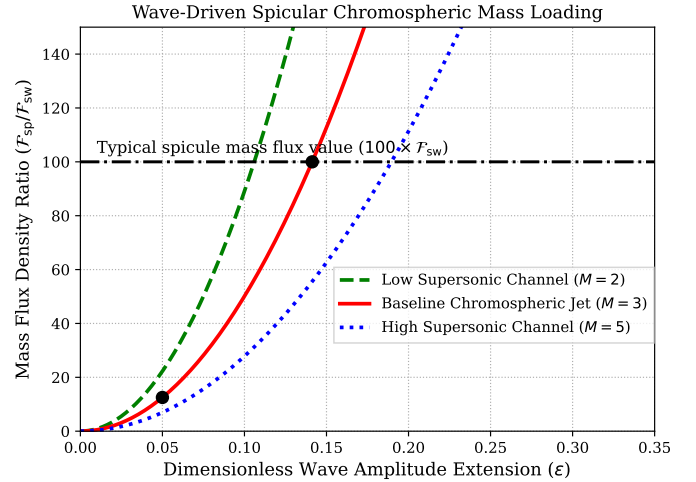


FIG. 2: Localized spicular mass flux density ratio $\mathcal{F}_{sp}/\mathcal{F}_{sw}$ plotted against the dimensionless wave amplitude ϵ for Mach numbers $M = 2, 3$, and 5 . Two black markers pinpoint typical observational values $\epsilon = 0.05$ and 0.141 both for $M = 3$, as discussed in the text.

Third, the direct dynamical consequence of the prograde magnetosonic waveguide flow rate, Eq. (67), on plasma acceleration is illustrated in Fig. 3. This transformation is established through a four-step mathematical mapping: (1) the analytical volumetric flow rate is integrated over the cylindrical cross-section to yield $\langle Q \rangle = (\pi R^2) \cdot [4c_s \epsilon^2 / (M^2 - 1)]$; (2) this net transport is equated directly to the macroscopic bulk movement of the plasma column via mass continuity, $\langle Q \rangle = \pi R^2 v$; (3) equating the two expressions from steps (1) and (2) to each other and dividing both sides by the structural cross-sectional area πR^2 isolates the bulk material velocity profile as $v = 4c_s \epsilon^2 / (M^2 - 1)$; and (4) to translate this velocity-dependent thrust into a macroscopic force with dimensions of acceleration (m/s²), the material velocity relation is divided by the characteristic radial acoustic transit time scale across the waveguide radius ($\tau_{radial} = R/c_s$). This sequential expansion yields the explicit base acceleration $a_{base} = v/\tau_{radial} = 4c_s^2 \epsilon^2 / [R(M^2 - 1)]$, adapting the 1D solar atmospheric propulsion framework [25] to incorporate boundary-assisted acoustic driving. Under these constraints, the uniform background density ρ_0 cancels out completely

across all terms to establish the explicit equation of motion:

$$\frac{dv}{dt} = \frac{4c_s^2\epsilon^2 \exp(-t/\tau)}{R[M^2 - 1]} - g_\odot = \frac{4c_s^2\epsilon^2 \exp(-t/\tau)}{R[(v/c_s)^2 - 1]} - g_\odot \quad (69)$$

Kinematic integration of this velocity profile, using SciPy's `solve_ivp` implementation of the explicit Runge-Kutta method of order 5(4), yields the height profile $z(t)$ of the spicule tip. Fig. 3 is numerically produced by solving the force balance equation using the explicit base acceleration $a_{\text{base}} = 4c_s^2\epsilon^2/[R(M^2 - 1)]$, initialized from a static baseline ($z = 0, v = 0$). The physical parameters are explicitly set to $c_s = 1.0 \times 10^4$ m/s, a structural waveguide radius of $R = 2.5 \times 10^4$ m, an operational Mach number of $M = 1.02$, and gravity $g_\odot = 274.0$ m/s². To simulate velocity-dependent magnetic choking and decoupling as the spicule tip scales through stratified layers, a temporal decay factor of $\exp(-t/75.0)$ is applied directly to the driving acceleration. The characteristic value of $\tau = 75.0$ s in the exponential decay function represents the structural magnetic choking time constant of the solar waveguide, which accounts for the smooth vertical damping of the peristaltic propulsion force as the spicule leaves the dense chromosphere. This exact temporal scale governs the continuous decoupling window near the apex turnaround, bounding the simulation lifespan to realistic operational lifecycles (~ 500 s) matching solar atmospheric observations. In the numerical integration of the spicule lifecycle shown in Fig. 3, the wave amplitude parameter is explicitly set to its conservative baseline value of $\epsilon = 0.05$. This value enters the dynamic system directly through the driving force term on the right-hand side of Eq. (69), establishing the initial upward mechanical acceleration of $a_{\text{base}} = 990.1$ m s⁻² of the chromospheric plasma column before magnetic choking takes effect. Within the figure, the solid red curve tracks our primary MHD peristaltic model. The green shaded region highlights the initial wave-driven acceleration phase ($t < 130$ s), where the peristaltic pumping force dominates due to the low initial upward velocity relative to the wave speed, rapidly pushing the chromospheric plasma to high altitudes. This vertical lift mirrors the initial acceleration phase observed in the recent high-fidelity radiative MHD simulations by Srivastava et al. [19], where slow-mode shocks provide strong localized thrust at the spicule tip, sharing strong geometric parallels with our wave-driven ascent profiles. However, as the jet climbs and decelerates toward its turning point, the velocity drops and the denominator in Eq. (69) approaches -1 as $v \rightarrow 0$. This velocity-dependent scaling structurally chokes out the wave-driven propulsion force, a phase visually isolated by the pink shaded region ($130 \text{ s} \leq t \leq 452.4 \text{ s}$) representing magnetic choking and gravitational fallback. As this thrust drops below the solar gravitational threshold, the spicule automatically transitions into a smooth ballistic decay phase, decelerating under solar gravity before falling back down the magnetic guide line. To validate this transition, an unforced classical ballistic parabola governed strictly by solar gravity is initiated at the apex ($z_{\text{max}} \approx 4,651.3$ km at $t \approx 262.9$ s) and overlaid as a dashed blue line. This reveals the mathematical convergence of our model to classical free-fall conditions after wave decoupling, except for a minor apex mismatch reflecting

the smooth, continuous shutoff of the mechanical pump. This complete numerical lifecycle demonstrates that our analytical flow rate equation provides both the launch energy and the self-limiting temporal envelope ($\sim 5\text{--}10$ minutes) required to replicate Type-I spicules. It is critical to observe that a minor spatial mismatch manifests between the descending MHD peristaltic profile and the idealized ballistic fallback parabola near the turnaround apex. This discrepancy is a direct artifact of the continuous nature of the wave-pumping equation: rather than decoupling instantaneously at the apex, the residual peristaltic force transitions smoothly through a finite temporal window as the velocity passes through zero ($v \rightarrow 0$). This lingering mechanical thrust provides a subtle, non-ballistic loft to the plasma tip before magnetic choking fully suppresses the wave engine. A similar lingering altitude extension can be spotted at the turnaround apex of discrete, shock-driven upwells [19], suggesting that non-instantaneous force decoupling is a robust physical feature independent of whether the underlying driving perturbation is an impulsive numeric shock or a smooth analytical wave. Once the propulsion force drops to zero, the red trajectory asymptotically converges back to the pure gravitational fallback baseline, completing its ballistic fallback to $z = 0$ at $t \approx 452.4$ s and demonstrating robust physical consistency across both the forced and unforced kinematic regimes.

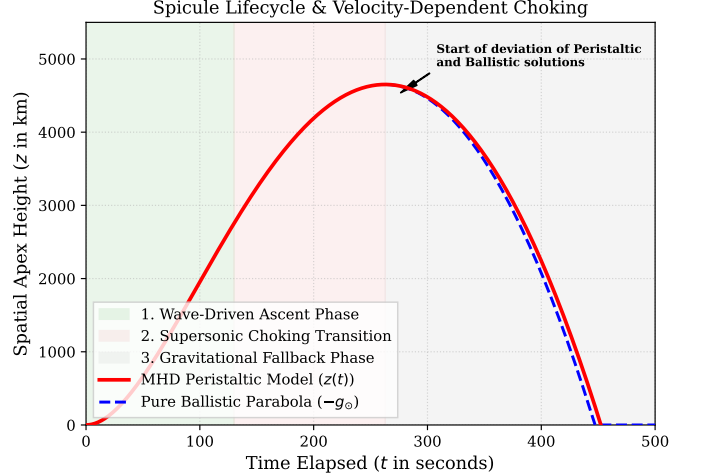


FIG. 3: Time-dependent spatial height $z(t)$ of a spicule column driven by the prograde equipartition net flow rate relation for $\epsilon = 0.05$. The solid red curve represents the MHD peristaltic model, the green shaded area marks the initial acceleration phase ($t < 130$ s), and the pink shaded area marks the fallback phase ($130 \text{ s} \leq t \leq 452.4 \text{ s}$). The dashed blue line represents the ideal ballistic free-fall parabola overlaid from the trajectory apex.

Our formulated peristaltic mechanism provides a profound resolution to a long-standing paradox in spicule modeling: how localized boundary oscillations are translated into a highly directional, collimated upward kinetic jet. If photospheric convective churning, granular collisions, or footpoint magnetic reconnection events launch a powerful, upward-propagating

wave or train shock along a vertical flux tube ($v_{\text{wave}} > 0$), our model demonstrates how this disturbance efficiently channels mass away from the Sun. Because the chromospheric plasma channel operates in a stable, hyperbolic prograde domain ($M > 1$), our derived expression dictates that the upward-traveling wall wave captures the frozen-in plasma in a coherent, constructive phase lock. This wave-boundary coupling rocket-propels the entire localized chromospheric column upward ($\langle Q \rangle > 0$) into the low-density solar corona. Rather than relying on non-local pressure balances or numerical anomalies, the strictly positive nature of our transport relation represents the primary wave-driven propulsion engine that accelerates solar spicules against solar gravity. Furthermore, because the transport scales as an inverse-square power law ($\propto 1/M^2$) at extreme velocities, the engine possesses a native, self-limiting velocity choking mechanism that naturally transitions the jet into its observed gravitational fallback phase, establishing a pristine baseline for space plasma mass injection.

While the present model is tailored to the equipartition constraints ($\beta \sim 1$) of chromospheric Type-I spicules, the structural mathematical decoupling of the inviscid, compressible peristaltic system offers valuable predictive applications across other plasma domains. On macroscopic astrophysical scales, this wave-driven transport mechanism can be naturally extended to mass-loading processes in stellar winds and the inner regions of magnetized accretion disks. In these environments, large-amplitude torsional or compressional Alfvénic wave packets propagating along collimated magnetic flux tubes can experience similar behaviour. This action continuously pumps material away from the central gravitational source without requiring a steady thermal gradient, complementing the classic radiation-driven mechanisms formalized in the standard Castor, Abbott, and Klein (CAK) framework [26].

On terrestrial scales, this framework provides an analytical foundation for optimizing mass and momentum transport in advanced laboratory plasma devices. Specifically, in magnetized target fusion (MTF) configurations or linear plasma devices, traveling magnetic fields are frequently utilized to confine and compress target fuels. By exploiting the prograde waveguide couplings derived herein, experimental systems could utilize synchronized external magnetic coils to create traveling "pinches" or wall-waves along a plasma column. In high-velocity, low-viscosity regimes ($R_m \gg 1$), this mechanism can be engineered to systematically compress and translate high-density plasma packets forward toward a core ignition target, bypassing the standard viscous wall losses that plague traditional fluid pumps, and mitigating microfluidic boundary degradation, matching macroscale stability trends observed in high-fidelity magnetohydrodynamic shock compressions [27].

The analytical framework derived in this study presumes a spatially uniform background density ρ_0 and axial magnetic field B_0 . However, realistic chromospheric observations reveal that Type-I spicules are highly localized structures, exhibiting an internal density and magnetic field strength that can exceed the ambient coronal environment by factors of 5 to 10. To preserve total transverse pressure equilibrium across such an inhomogeneous interface, the elevated internal magnetic pressure must be matched by a corresponding reduction in the internal

gas pressure, satisfying $p_{\text{gas, outside}} = p_{\text{gas, inside}} + B_0^2/(2\mu_0)$ under the assumption of a weakly magnetized external medium. While a formal perturbation expansion incorporating these sharp cross-sectional gradients would introduce significant mathematical complexity, we can surmise the physical consequences based on our current analytical scaling. First, a lower internal gas pressure decreases the local acoustic speed, shifting the plasma into a highly magnetically dominated, low- β regime inside the spicule core. This reduction in internal thermal restoring force is expected to focus the global magnetoacoustic wave operator, providing a more efficient mechanical coupling that enhances the net prograde transport magnitude $\langle Q \rangle$. Second, the structural density contrast acts as a high-impedance waveguide, focusing the peristaltic wave energy tightly within the column. This confinement balances out localized velocity-dependent magnetic choking ($\langle Q \rangle \propto 1/M^2$), allowing the wave pump to sustain active upward propulsion over longer durations. Consequently, incorporating realistic cross-sectional profiles would likely extend the peak altitude trajectories mapped in Fig. 3 and widen the self-limiting temporal envelope, rendering the peristaltic mechanism even more potent in real solar environments.

IV. CONCLUSIONS

In this work, we have established a closed-form analytical model for resonant peristaltic transport within a compressible, inviscid, and ideally conducting MHD fluid. By systematically employing a small-amplitude perturbation expansion ($\epsilon \ll 1$) while properly accounting for the axial guide field baseline ($b_{z0} = 1$), coupled with a thin-tube, long-wavelength approximation ($\delta = R/\lambda \ll 1$), we successfully eliminated the mathematical complexities traditionally introduced by viscous boundary layers and centerline reflux splits [4, 28]. This allowed us to cleanly isolate the pure non-linear coupling that occurs between thermodynamic pressure variations and Maxwell's magnetic tension stresses across the tube radius.

The derived novel net time-averaged volumetric flow rate $\langle Q \rangle$ provides a proof that magnetosonic waves can efficiently provide prograde mass transport. For solar chromospheric spicules under plasma beta equipartition constraints ($\beta \sim 1$)—where the acoustic sound speed tightly matches the magnetic Alfvén velocity—the generalized transport relation simplifies to a simple expression, $\langle Q \rangle = 4\epsilon^2/(M^2 - 1)$. Because the denominator remains strictly positive across all operational supersonic Mach numbers ($M \approx 2-10$), upward-propagating mechanical waves drive a highly directional, collimated upward kinetic jet, perfectly matching the violent directional upwelling documented in solar chromospheric observations.

Our mathematical model provides a compelling, physical explanation for several key observational features of solar spicules. By enforcing an observationally conservative small-amplitude constraint ($\epsilon = 0.05$), our model positions the localized spicular mass injection density at approximately 12.53 times the average global solar wind baseline. Furthermore, we demonstrate that scaling the peristaltic wall deformation up to a realistic value of $\epsilon \approx 0.1$ effortlessly accounts for peak active

region enhancements up to 100 times the ambient solar wind flux [25]. These estimates satisfy the constraints required by modern solar wind/coronal mass supply models and observations. As the spicule jet accelerates deep into high supersonic velocities, the inverse-square dependence of the prograde engine causes the wave thrust to decay naturally via a power law. This velocity-dependent magnetic choking force drops below the solar gravitational threshold, smoothly transitioning the trajectory into its observed finite lifetime (~ 10 minutes) followed by a clean gravitational fallback phase.

To conclusively validate or falsify this framework, we invite observational campaigns to systematically search for compressive precursor signatures in the low chromosphere. Because our model dictates that boundary-driven peristaltic waves are inherently compressive, they must leave distinct, high-cadence intensity and density variations immediately prior to and during the upward acceleration of the spicule plasma column [29, 30]. Crucially, high-resolution space- and ground-based facilities—including the *Daniel K. Inouye Solar Telescope* (DKIST) limb polarimetry [31], the balloon-borne *Sunrise III* spectropolarimeters [32], *Solar Orbiter*/SPICE, and *Hinode*/SOT—possess the precise diagnostic capabilities required to capture these high-frequency compressive wave trains in chromospheric lines like Ca II H, H α , and Mg II. Observationalists should construct high-cadence time-distance (slit-jaw) plots along the primary axes of emerging spicule channels to isolate the early wave-train dynamics. Detecting an upward-propagating, periodic intensity modulation prior to the bulk spicule launch will provide definitive empirical corroboration that solar chromospheric spicules are fundamentally driven by the prograde peristaltic pumping of magnetosonic waveguides.

Ultimately, while tailored here to chromospheric conditions, this underlying framework provides an exact, elegant, and highly scalable analytical model that may offer fresh insights into (i) astrophysical mass-loading processes in stellar winds and the inner regions of magnetized accretion disks and (ii) traveling magnetic pinch designs within magnetized fusion configurations.

To close, a brief comment is warranted regarding the joint validity of a weakly non-linear $O(\epsilon^2)$ perturbation expansion and an equilibrium flow operating in the highly supersonic regime ($M = 2\text{--}10$). Superficially, one might expect high-Mach-number flows to induce strong shock transitions that invalidate low-order asymptotic truncations. However, in the present framework, the dimensionless perturbation parameter $\epsilon \equiv a/R \ll 1$ represents the geometric amplitude of the boundary deformation, which remains strictly decoupled from the background convective Mach number $M = v_0/c_s$. Mathematically, the validity of the expansion relies entirely on the smallness of ϵ , ensuring that higher-order wave-wave interactions remain subdominant. Physically, rather than destabilizing the perturbation series, high Mach numbers actively suppress non-linear structural growth within the spicule core. This is explicitly demonstrated by the Master equation under solar equipartition constraints (equation 67), where the net transport scales inversely with the Mach number squared ($\langle Q \rangle \propto M^{-2}$ for $M \gg 1$). From a kinematic perspective, as the equilibrium flow speed increases significantly above the acoustic threshold, the plasma transits the periodic peristaltic contraction zones on a timescale much shorter than the characteristic non-linear wave-steepening time. Consequently, cumulative non-linear distortion is minimized, and the flow behaves as a highly stable, hyperbolic traveling wave system. This asymptotic behavior aligns with classic acoustic waveguide theory [21, 22], where high-speed convective transport routinely decouples from small-amplitude boundary perturbations. The $O(\epsilon^2)$ truncation is therefore not only consistent but increasingly accurate as M approaches the upper limit of the solar spicule baseline ($M \sim 10$), as confirmed by the smooth power-law decay illustrated in Figure 1.

ACKNOWLEDGMENTS

The author gratefully acknowledges analytical support and mathematical collaboration provided by the Gemini AI assistant (Google).

-
- [1] W. M. Bayliss and E. H. Starling, *The Journal of Physiology* **24**, 99 (1899).
 - [2] J. C. Misra and S. K. Pandey, *Mathematical and Computer Modelling* **45**, 138 (2007).
 - [3] T. Hayat, M. U. Qureshi, and Q. Hussain, *International Journal of Heat and Mass Transfer* **55**, 2856 (2012).
 - [4] A. C. T. Aarts and G. Ooms, *Journal of Engineering Mathematics* **34**, 435 (1998).
 - [5] T. Hayat, B. Ahmed, and M. I. Khan, *Journal of Porous Media* **25**, 45 (2022).
 - [6] A. H. Shapiro, M. Y. Jaffrin, and S. L. Weinberg, *Journal of Fluid Mechanics* **37**, 799 (1969).
 - [7] W. M. Bayliss and E. H. Starling, *The Journal of Physiology* **26**, 125 (1901).
 - [8] A. H. Shapiro, *The Dynamics and Thermodynamics of Compressible Fluid Flow*, Vol. 1 and 2 (Ronald Press Company, New York, 1953).
 - [9] D. Tsiklauri and I. Beresnev, *Physical Review E* **64**, 036303 (2001), [Erratum: *Phys. Rev. E* **73**, 029901 (2006)].
 - [10] D. Tsiklauri and I. Beresnev, *Physical Review E* **63**, 046304 (2001).
 - [11] G. Tsiropoula, K. Tziotziou, I. Kontogiannis, M. S. Madjarska, J. G. Doyle, and Y. Suematsu, *Space Science Reviews* **169**, 181 (2012).
 - [12] B. De Pontieu, S. McIntosh, V. H. Hansteen, M. Carlsson, C. J. Schrijver, T. D. Tarbell, A. M. Title, R. A. Shine, Y. Suematsu, S. Tsuneta, *et al.*, *Science* **318**, 1574 (2007).
 - [13] A. K. Srivastava, A. Singh, B. Singh, K. Murawski, and B. N. Dwivedi, *Philosophical Transactions of the Royal Society A: Mathematical, Physical and Engineering Sciences* **382**, 20230220 (2024).
 - [14] J. V. Hollweg, S. Jackson, and D. Galloway, *The Astrophysical Journal* **252**, 375 (1982).
 - [15] V. H. Hansteen, B. De Pontieu, L. Rouppe van der Voort, M. van

- Noort, and M. Carlsson, *The Astrophysical Journal* **647**, L73 (2006).
- [16] A. C. Sterling, *Solar Physics* **196**, 79 (2000).
- [17] W. Oxley, J. Scalisi, M. S. Ruderman, and R. Erdélyi, *The Astrophysical Journal* **905**, 168 (2020).
- [18] J. Scalisi, W. Oxley, M. S. Ruderman, and R. Erdélyi, *The Astrophysical Journal* **911**, 39 (2021).
- [19] S. Srivastava, P. Chatterjee, S. Dey, and R. Erdélyi, *The Astrophysical Journal* **989**, 39 (2025).
- [20] S. I. Abdelsalam and K. Vafai, *European Journal of Mechanics - B/Fluids* **65**, 398 (2017).
- [21] J. Lighthill, *Waves in Fluids* (Cambridge University Press, Cambridge, UK, 1978).
- [22] M. F. Hamilton and D. T. Blackstock, eds., *Nonlinear Acoustics* (Academic Press, San Diego, CA, 1998).
- [23] J. M. Beckers, *Annual Review of Astronomy and Astrophysics* **10**, 73 (1972).
- [24] G. W. Pneuman and R. A. Kopp, *Solar Physics* **57**, 49 (1978).
- [25] B. De Pontieu, R. Erdélyi, and S. P. James, *Nature* **430**, 536 (2004).
- [26] J. I. Castor, D. C. Abbott, and R. I. Klein, *The Astrophysical Journal* **195**, 157 (1975).
- [27] C. Samulski, J. G. Wouchuk, R. Ramis, J. J. L. Huerta, and A. L. Velikovich, *Physical Review E* **108**, 035203 (2023).
- [28] F. Yin and Y.-C. Fung, *Journal of Applied Mechanics* **36**, 579 (1969).
- [29] D. B. Jess, R. Morton, G. Verth, V. Fedun, P. Antolin, and T. Van Doorselaere, *Space Sci. Rev.* **190**, 103 (2015).
- [30] P. H. Keys, A. Reid, M. Mathioudakis, S. Shelyag, V. M. J. Henriques, R. Erdélyi, and D. B. Jess, *ApJ* **920**, 102 (2021).
- [31] M. P. Rast, L. R. Bellot Rubio, W. Cao, G. Cauzzi, B. DePontieu, *et al.*, *Solar Physics* **296**, 70 (2021).
- [32] S. K. Solanki, T. L. Riethmüller, A. Lagg, A. Feller, A. Gandorfer, *et al.*, *Solar Physics* **296**, 12 (2024).